Biosensors and Bioelectronics 304 (2026) 118572

Contents lists available at ScienceDirect

Biosensors and Bioelectronics

journal homepage: www.elsevier.com/locate/bios

Calibration-free potassium quantification via a stoichiometric enzyme cascade on laser-induced graphene

Chaeeun Kim [a], Chaehyung Kim [a], Yujoon Kim [a], Kangwon Lee [a,b,*]

[a] Department of Applied Bioengineering, Graduate School of Convergence Science and Technology, Seoul National University, Seoul, 08826, Republic of Korea
[b] THEDONEE Inc., Research Center, Seoul, Republic of Korea

ARTICLE INFO

Keywords:
Amperometric sensor
Potassium-ion sensing
Bienzymatic biosensor
Laser-induced graphene
Point-of-care testing

ABSTRACT

Potassium (K^+) monitoring is essential for clinical management, particularly for point-of-care testing (POCT) that requires rapid and reliable analysis. Conventional potentiometric ion-selective electrodes rely on equilibrium potential responses and frequent calibration, which limits their applicability in decentralized testing. Here, we present an amperometric K^+ biosensor based on a pyruvate kinase/oxidase (PK/POx) enzyme cascade integrated with a laser-induced graphene (LIG) electrode. K^+-dependent enzymatic activity is converted into a direct current signal via 4-nitrosoaniline-mediated redox cycling. The porous, defect-rich LIG architecture acts as a reaction-accelerating electrochemical interface that facilitates enzymatic turnover and mediator-assisted electron transfer. Under optimized conditions, the sensor exhibited a linear response over the physiological range of 2–8 mM, a detection limit of 1.56 mM, high selectivity against interfering ions, excellent inter-sensor reproducibility (RSD = 2.41–5.20%), and reliable performance in spiked human serum samples. By operating in a rate-governed, current-mode sensing framework rather than an equilibrium-based potential measurement, the PK/POx/LIG platform enables point-of-use operation without requiring sensor-specific or user-performed calibration at the time of measurement, enabling rapid potassium monitoring in POCT applications.

1. Introduction

Potassium (K^+) is an essential electrolyte that supports key physiological functions, including the maintenance of intracellular and extracellular ionic balance, muscle contraction, neuronal signal transmission, and cardiac rhythm regulation (Zacchia et al., 2016). Blood K^+ levels must be precisely maintained within the normal range (3.5–5.0 mM), and out of this range can lead to serious physiological abnormalities such as arrhythmia, muscle weakness, impaired neurotransmission, and life-threatening hyperkalemia (Viera and Wouk, 2015). Patients with chronic kidney disease (CKD), particularly those undergoing dialysis, are especially vulnerable to rapid K^+ fluctuations due to impaired renal excretion, making timely potassium monitoring clinically critical (Baxter et al., 2022). These clinical challenges underscore the growing need for point-of-care testing (POCT) platforms capable of quickly and accurately measuring blood K^+ concentrations (Park et al., 2025).

Although optical, fluorescent, and colorimetric sensing methods have been explored for biochemical analysis (Lee et al., 2010; Kim et al., 2021; Lee et al., 2022), these techniques typically require bulky optical components, precise alignment, and multi-step reagent handling, which limit their suitability for POCT. In contrast, electrochemical biosensors offer inherent advantages for point-of-care applications, including ease of miniaturization and low manufacturing cost (Wang, 2006, Bambang Kuswandi et al., 2025). They also respond quickly to small samples and operate with simple electronic circuits, making them suitable for portable devices and real-world clinical settings. Various electrochemical biosensor designs have adopted enzymatic cascades, redox mediators, and current-mode transduction to enhance sensitivity and support calibration-free operation (Liu et al., 2021).

Electrochemical ion sensors can be classified into potentiometric and amperometric systems. Despite the availability of multiple transduction strategies, most clinically used potassium sensors still rely on potentiometric ion-selective electrodes, which generate voltage signals based on ion activity (Gao et al., 2016; Hutter et al., 2022). Despite their widespread clinical adoption, this voltage-based sensing paradigm remains intrinsically vulnerable to signal drift, necessitating frequent calibration and stabilization to ensure reliable operation. These requirements impose fundamental constraints in POCT environments, where rapid,

* Corresponding author. Department of Applied Bioengineering, Graduate School of Convergence Science and Technology, Seoul National University, Seoul, 08826, Republic of Korea.
E-mail address: kangwonlee@snu.ac.kr (K. Lee).

https://doi.org/10.1016/j.bios.2026.118572
Received 19 December 2025; Received in revised form 23 February 2026; Accepted 27 February 2026
Available online 6 March 2026

robust measurements with minimal user intervention are required (Marc Parrilla and Crespo, 2019).

In contrast, amperometric sensing represents a fundamentally different, current-mode sensing paradigm, in which analytical signals are governed by reaction rates rather than equilibrium potentials. By directly measuring current signals proportional to reaction kinetics, amperometric systems enable fast response, high signal-to-noise ratios, and simplified measurement protocols without prolonged stabilization. From a transduction standpoint, current-mode sensing provides a rate-governed framework in which analytical readout is determined by reaction kinetics rather than equilibrium potential formation. When combined with predefined and fixed assay conditions, such a framework allows potassium concentration to be directly inferred from the measured current at the point of use (Sassolas et al., 2008; Ma et al., 2021).

This approach is particularly strengthened when combined with an enzyme-based sensing strategy that converts ion concentration changes into changes in enzyme reaction rates and reads them as electrochemical signals. In this context, pyruvate kinase (PK) shows K^+-dependent activation, and accordingly (Oria-Hernández et al., 2005), the PK/POx enzyme cascade can serve as a biochemical transducer to convert K^+ concentration changes into electrochemically measurable current signals.

The performance of electrochemical enzymatic sensors is strongly influenced by the electron-transfer efficiency of the mediator and the physicochemical properties of the electrode interface. Efficient mediator redox cycling requires electrodes with high conductivity, large surface area, and abundant electrochemically active sites (Lee et al., 2025). Carbon-based electrodes inherently satisfy these criteria and have therefore been widely adopted in biosensor applications. Among the available fabrication methods, direct laser writing (DLW), which converts polyimide (PI) into laser-induced graphene (LIG) via localized pyrolysis, provides a mask-free and scalable route for fabricating high-performance carbon electrodes (Jian Lin et al., 2014; Movaghgharnezhad and Kang, 2024). Recent studies have shown that LIG can facilitate complex electrocatalytic and biochemical reactions, including nitrate electroreduction and glucose-driven biosensing (Geng et al., 2024; Gu et al., 2025), underscoring its functional versatility in both analytical and therapeutic applications. These findings collectively underscore the promise of DLW-fabricated LIG for biosensing platforms (Liu et al., 2022).

LIG exhibits a porous three-dimensional structure, high defect density, excellent electrical conductivity, and a large electroactive surface area, all of which are highly advantageous for enzyme immobilization and mediator-facilitated electron transfer (Gao et al., 2021; Mingyang Liu et al., 2023). In addition, DLW enables mask-free and chemical-free digital patterning of user-defined electrode geometries and is compatible with roll-to-roll manufacturing (Luong et al., 2019). These characteristics make LIG a promising platform for high-throughput and low-cost fabrication of disposable biosensors (Ye et al., 2019).

To the best of our knowledge, this study reports the first amperometric potassium biosensor that directly converts K^+ concentration changes into current signals through a stoichiometrically governed enzyme-kinetic transduction mechanism. Here, we integrate a PK/POx enzyme cascade with a LIG electrode to establish a current-mode potassium sensing platform tailored for POCT. The technical validity of this platform is systematically demonstrated through electrode fabrication, surface characterization, enzyme immobilization, mediator-assisted electron-transfer analysis, and comprehensive evaluation of its analytical performance.

2. Experimental

2.1. Reagents and materials

Pyruvate Kinase (PK, EC 2.7.1.40), Pyruvate Oxidase (POx, EC 1.2.3.3), Poly(ethylene oxide) (PEO), Adenosine 5′-diphosphate sodium salt (ADP-Na), Phosphoenolpyruvate tri(cyclohexylammonium) salt (PEP), 4-nitrosoaniline (4-NA), Triton X-100, Iron(III) Chloride, Lithium dihydrogen phosphate, Magnesium sulfate, Glycerol, Tris-HCl buffer (pH 7.0), Potassium chloride (KCl), Human serum and Ag/AgCl paste (113-09) were purchased from commercial suppliers and used as received. All aqueous solutions were prepared using ultra-pure water (>18 MΩ·cm).

2.2. Biosensors fabrication

2.2.1. Fabrication of laser-induced graphene electrodes

LIG electrodes were fabricated by directly converting the surface of a 0.125 mm Polyimide (PI) film using a CO_2 laser (10.6 μm, Universal VLS 3.60DT). The electrode platform consisted of a three-electrode configuration comprising a working electrode (WE), a counter electrode (CE), and a reference electrode (RE). Two sequential laser irradiation steps were applied to the same PI surface using distinct laser power and scan rate settings. The first irradiation, a power of 4.2 W and a scan rate of 127 mm s^{-1} were applied, whereas the second irradiation employed 2.4 W and 228.6 mm s^{-1}. A defocus distance of 0.1 mm at 1000 pulses per inch (p.p.i.) was maintained during both steps to obtain uniform LIG patterning. This two-step irradiation strategy was adopted to ensure deeper graphitization and improved surface uniformity, which were not achievable with a single laser pass.

Ag paste was screen-printed only onto the RE as a precursor for Ag/AgCl formation and onto the contact pads to reduce interfacial connection resistance. The Ag layer on the RE was then converted to Ag/AgCl form by $FeCl_3$ treatment to yield a stable reference electrode for electrochemical measurements.

2.2.2. Fabrication of PK/POx/LIG biosensors

The PK/POx-based K^+ amperometric biosensor was prepared on the LIG working electrode described in Section 2.2.1. A sensing formulation containing pyruvate kinase (PK), pyruvate oxidase (POx), the redox mediator 4-nitrosoaniline (4-NA), and substrate components (LiH_2PO_4, $MgSO_4$, ADP, and PEP) was prepared from concentrated stock solutions. A 2% (w/v) PEO solution was included as a film-forming matrix. The sensing mixtures were prepared using the same procedure, differing only in the variable under investigation (mediator concentration, PK:POx ratio, or ADP:PEP ratio). Prior to deposition, the LIG electrode was treated with oxygen plasma (15W, 10 s, O_2 flow rate: 10 sccm, chamber pressure: 1 Torr; Femto Science Co., Ltd) to enhance surface hydrophilicity. The sensing mixture was static-cast onto the LIG surface and dried under ambient conditions to form the enzyme layer. To ensure consistent immobilization, a fixed volume (2.5 μL) of enzyme solution was applied per strip, followed by ambient drying under controlled humidity (30%).

2.3. Characterization

The morphology of the LIG was characterized by field-emission scanning electron microscopy (FE-SEM, SIGMA 360). Surface wettability was assessed by static water contact angle measurements using a contact angle meter (UNI-CAM.A). Raman spectra were acquired using a system equipped with a 532 nm laser and 700 lines/mm grating. Electrochemical characterization was performed using a CH Instruments 660E electrochemical workstation in a three-electrode configuration (working, reference, counter electrodes) and included electrochemical impedance spectroscopy (EIS) and cyclic voltammetry (CV).

2.4. Electrochemical measurements

Prior to amperometric measurements, linear sweep voltammetry (LSV) was performed to determine the operating potential of the PK/POx/LIG electrode. Based on this preliminary analysis, an applied po-

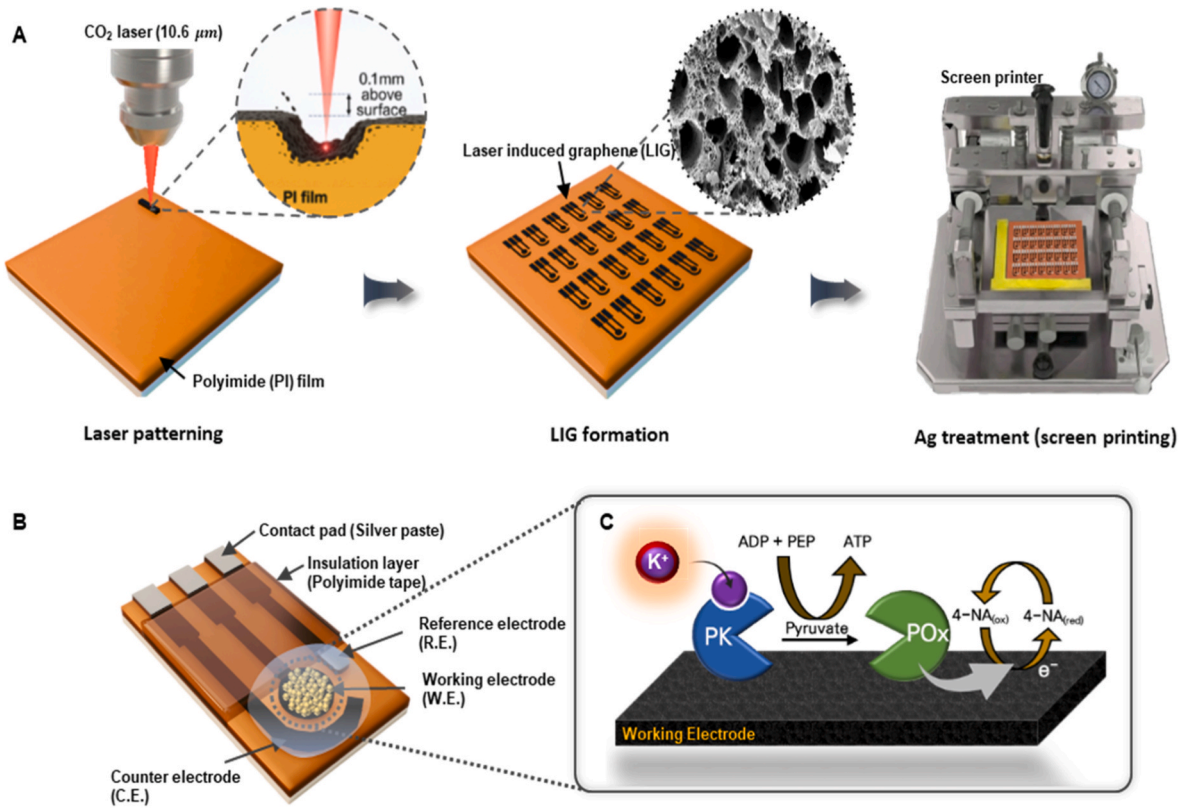

Fig. 1. Schematic of PK/POx/LIG potassium biosensor.
A) Fabrication of the LIG electrode through CO2 laser irradiation on a polyimide substrate, followed by Ag treatment for the reference electrode (RE) and contact pads; B) Schematic illustration of the three-electrode LIG platform consisting of a working, reference, and counter electrode with Ag contact pads; C) K^+-activated PK/POx enzyme cascade on the LIG working electrode, in which K^+-dependent activation of pyruvate kinase generates pyruvate that is subsequently oxidized by pyruvate oxidase, driving 4-NA redox cycling and producing an amperometric signal.

tential of 0.9 V was selected for all subsequent chronoamperometric measurements. All amperometric measurements were performed in a KCl buffer under static conditions without external stirring. For each measurement, 200 μL of electrolyte solution containing the target K^+ concentration was static cast onto the sensor strip, and the current response was recorded at room temperature. The analytical current was defined as the chronoamperometric current measured at 5 s after potential application, excluding the initial capacitive transient (≈ 1–3 s). The same fixed-time criterion was applied throughout all optimization and calibration experiments.

2.5. Optimization of sensing parameters

2.5.1. Effect of mediator concentration

To evaluate the effect of 4-NA concentration on the PK/POx-based K^+ amperometric response, only the mediator concentration was varied while all enzyme and substrate components were kept constant. A 2x substrate cocktail was prepared containing the 100 mM LiH_2PO_4, 16 mM $MgSO_4$, 10 mM ADP-Na, 30 mM PEP, 0.6% (w/v) PEO, 0.2% Triton X-100, and 4.4% glycerol. All components were mixed using the corresponding bulk stock solutions described above.

Reaction mixtures were formulated to yield final mediator concentrations of 10, 20, 30, 40, and 50 mM, while maintaining identical concentrations of PK, POx, substrates, and additives across all additions.

2.5.2. Enzyme ratio optimization (PK:POx)

Enzyme ratio optimization was performed by varying the relative activities of PK and POx while using the same 2x substrate cocktail described above, formulated with 20 mM 4-NA as the mediator. PK:POx ratios of 1:0.5, 1:1, 1:2, 1:3, 1:5, and 1:10 were examined. Reaction mixtures for each condition were prepared to achieve the designated enzyme ratio, while keeping all substrate and additive concentrations constant across conditions.

2.5.3. Optimization of substrate composition (ADP:PEP)

Optimization of the ADP:PEP ratio was conducted because the substrate composition determines the PK reaction rate and the amount of K^+-dependent pyruvate generated. The 2x substrate cocktail used in this experiment followed the same formulation described in Section 2.5.2, except that the ADP and PEP concentrations were adjusted according to the designated substrate ratios.

ADP:PEP ratio of 1:0.23, 1:0.5, 1:1, and 1:1.67 were evaluated, corresponding to final PEP concentrations of 0.7, 1.5, 3, and 5 mM. These concentrations were selected based on the reported Michaelis constant (K_m) values of ADP (0.3 mM) and PEP (0.07 mM), as substrate levels approximately tenfold higher than K_m are commonly used to maintain linear reaction kinetics (Pant, 2022).

3. Results and discussion

3.1. Laser-induced graphene electrode platform: fabrication and physicochemical characterization

The structural and electrochemical properties of LIG electrodes were evaluated to confirm their suitability as a biosensor platform. Field-emission scanning electron microscopy (FE-SEM) revealed that the LIG surface exhibited a highly porous and corrugated microstructure (Fig. 2A and B), suggesting a large accessible surface area favorable for biomolecule loading. To examine the effect of the laser irradiation strategy on LIG uniformity, surface morphologies obtained by single-

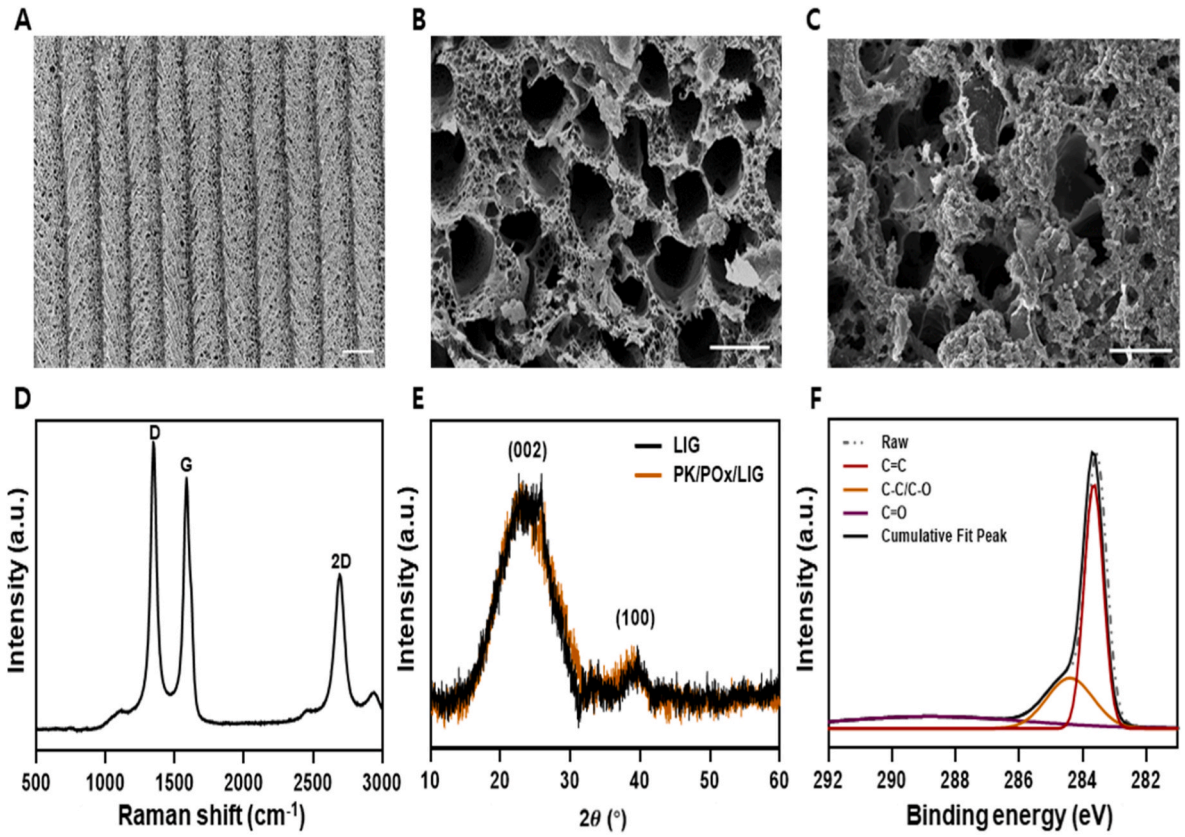

Fig. 2. Morphology and structural characterization
FE-SEM images of LIG at both (A) low (scale bar: 50 μm) and (B) high (scale bar: 5 μm) magnifications reveal a porous, wrinkled morphology, (C) while enzyme immobilization on the LIG surface following PK/POx static casting is visualized in the corresponding SEM image (scale bar: 5 μm); (D) Raman spectrum of LIG; (E) XRD pattern of powdered LIG; (F) High-resolution C 1s XPS spectrum of the LIG electrode, showing deconvoluted carbon bonding states (C=C/C-C, C-O, C=O), indicative of partial oxidation and defect formation during laser carbonization.

step and double-step laser irradiation were compared. As shown in Fig. S2, the double-step process produced a more uniform porous structure and well-defined electrode patterning. After static casting the PK/POx enzyme mixture, enzyme aggregates were broadly distributed across the LIG surface (Fig. 2C). Surface wettability was assessed by static contact angle measurements (UNI-CAM.A): the contact angle decreased from 119.5 ° for bare LIG to 13.68 ° after O_2 plasma treatment, and further to 6.77 ° after PK/POx immobilization, indicating a pronounced increase in surface hydrophilicity conductive to biomolecular immobilization (Fig. S4) (Datta et al., 2013).

The fabrication process and overall structure of the PK/POx/LIG biosensor are illustrated in Fig. 1. The polyimide (PI) substrate was converted into LIG by CO_2 laser irradiation (Fig. 1A), resulting in a microporous conductive carbon network. A three-electrode configuration consisting of a circular working electrode, a reference electrode, and a counter electrode was patterned on the same substrate, followed by the formation of a low-resistance Ag contact pad via screen printing to reduce external contact resistance (Fig. 1B, Fig. S1).

The graphitic structure and defect characteristics of the LIG electrode were examined by Raman spectroscopy (Fig. 2D). The Raman spectrum exhibited characteristic D (~1350 cm^{-1}), G (~1580 cm^{-1}), and 2D (~2700 cm^{-1}) bands, with I_D/I_G and I_{2D}/I_G ratios of 1.14 and 0.64, respectively, indicating a defect-rich structure composed of sp^2 carbon domains and few-layer graphene characteristics (Mingyang Liu et al., 2023). Such defect-rich graphitic structures increase the density of electrochemically active edge-plane sites, which facilitates faster electron transfer, while simultaneously providing abundant anchoring sites for enzyme immobilization (Tehrani and Bavarian, 2016). X-ray diffraction (XRD) analysis of powdered LIG (Fig. 2E) further confirmed the formation of multilayered graphitic domains, with distinct (002) and (100) peaks consistent with partially ordered graphene structures. High-resolution XPS analysis (Fig. 2F) supported these observations, with the C 1s spectrum exhibiting dominant sp^2 (C=C) peaks alongside oxygen-containing groups (C-O, C=O), reflecting partial oxidation during laser carbonization. To further elucidate the elemental composition of the LIG surface, survey XPS spectra were also analyzed, confirming the presence of carbon and oxygen species consistent with the high-resolution C 1s deconvolution results (Fig. S3). These structural and chemical features collectively suggest a conductive yet defect-rich carbon framework favorable for interfacial electrochemical processes.

The electrochemical properties of the LIG platform were evaluated by cyclic voltammetry (CV) and electrochemical impedance analysis (EIS). CV analysis in 5 mM $[Fe(CN)_6]^{3-/4-}$ with 0.1 M KCl revealed that Ag-modified contact pad LIG (Fig. 3B) exhibited increased redox peak currents and reduced peak-to-peak separation compared to bare LIG (Fig. 3A), indicating improved electron transfer kinetics. Randles-Ševčík plots (Fig. 3C) showed a linear relationship between peak current (Ip) and the square root of scan rate ($\sqrt{v}$), with the Ag-modified electrode exhibiting excellent linearity ($R^2 = 0.999$) and a steeper slope, suggesting an increased electroactive surface area (Yang et al., 2015). EIS measurements (Fig. 3D) further confirmed improved interfacial charge transfer, as the charge transfer resistance (R_{ct}) decreased significantly from 77.8 Ω for bare LIG to 34.0 Ω after Ag modification.

As summarized in Table S1, the LIG electrode exhibited a substantially lower sheet resistance (17.35 Ω sq^{-1}) and correspondingly higher electrical conductivity than carbon nanomaterial-based electrodes, which is expected to minimize internal ohmic losses and facilitate rapid electron collection across the porous electrode network, which is

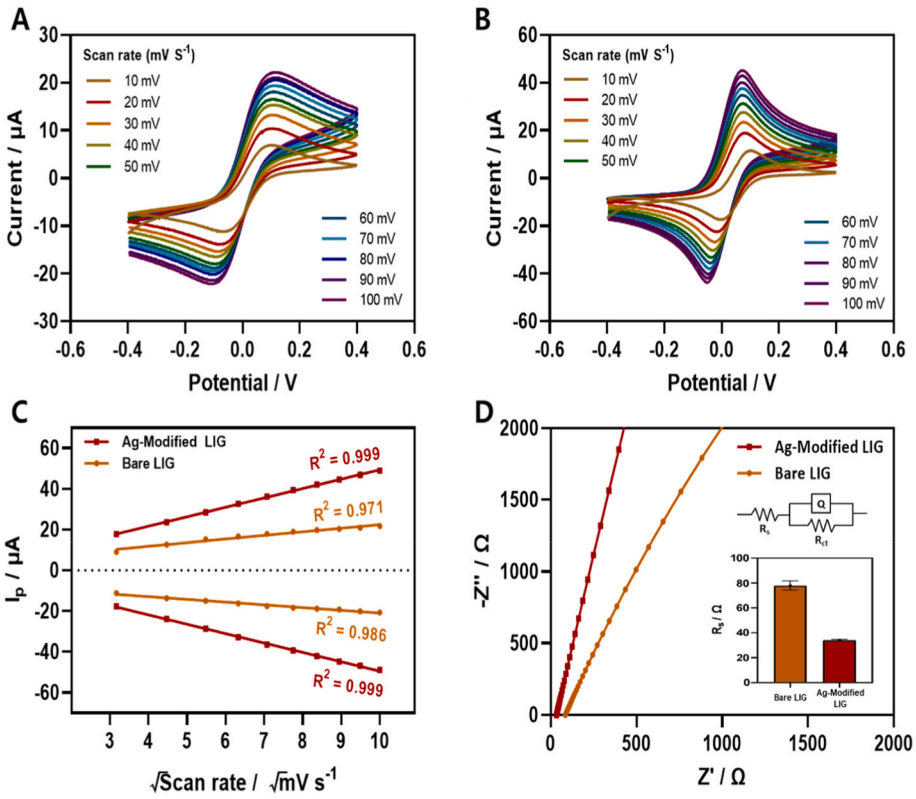

Fig. 3. Electrochemical characterization of the LIG electrode platform
Cyclic voltammograms of LIG electrode platform (A) without Ag-modified contact pads (bare LIG) and (B) with Ag-modified contact pads in 5 mM $[Fe(CN)_6]^{3-/4-}$ with 0.1 M KCl at scan rates of 10 – 100 mV s^{-1}, showing increased peak currents and reduced peak separation after Ag modification. (C) Randles-Šević k plots of anodic and cathodic peak currents versus $\sqrt{v}$, with higher slopes and strong linearity ($R^2 \approx 0.999$) for Ag-modified LIG. (D) Nyquist plots fitted with a CPE-based Randles circuit, indicating a substantial decrease in charge-transfer resistance (R_{ct}) after Ag modification (inset).
*Error bar represents the standard deviation (n = 4), calculated from independently measured electrode samples.

particularly advantageous for enzyme-based amperometric systems relying on continuous redox cycling. In this context, the LIG platform can be regarded as an electrode that supports accelerated electrochemical reaction kinetics rather than merely serving as a passive current collector.

Collectively, these results demonstrate that the LIG platform, with its unique porous morphology and enhanced electrochemical properties, provides a robust scaffold for enzyme immobilization and high sensitivity biosensing performance described in the subsequent sections.

3.2. Enzyme-kinetic current transduction via the PK/POx cascade on LIG

The sensing mechanism is governed by a K^+ activated PK/POx enzymatic cascade immobilized on the LIG working electrode. As shown in Fig. 1C, K^+ acts as an essential activator of PK, converting PEP and ADP into pyruvate and ATP. Since PK activity increases proportionally with K^+ concentration, the rate of pyruvate formation is directly regulated by the external K^+ level.

$$\mathrm{PEP} + \mathrm{ADP} \xrightarrow{PK,\ K^+,\ Mg^{2+}} \mathrm{pyruvate} + \mathrm{ATP} \qquad \text{(reaction 1)}$$

$$\mathrm{Pyruvate} + \mathrm{Phosphate} + 4-\mathrm{NA_{ox}} \xrightarrow{POx} \mathrm{Acetylphosphate} + 4-\mathrm{NA_{red}} \qquad \text{(reaction 2)}$$

$$4-\mathrm{NA_{red}} \rightarrow 4-\mathrm{NA_{ox}} + 2e^- + 2H^+ \qquad \text{(reaction 3)}$$

The pyruvate generated in reaction 1 is subsequently oxidized by POx (reaction 2), during which electrons are transferred directly to the redox mediator 4-NA. The reduced mediator (4-NA_{red}) is electrochemically reoxidized on the LIG surface under the applied potential (reaction 3), producing a measurable amperometric signal. Because reaction 1 and 2 are tightly coupled, the magnitude of the measured current is directly governed by the K^+-dependent activation of PK. This establishes the mechanistic basis by which external K^+ concentrations modulate pyruvate production and, consequently, the electron-transfer rate in the 4-NA redox cycle.

Maximizing the sensitivity of this K^+ reaction cascade requires careful optimization of several biochemical parameters, including the mediator concentration, PK:POx activity ratio, and substrate composition (ADP/PEP). These design considerations are systematically evaluated in Section 3.2.1.

3.2.1. Optimization of the PK/POx enzyme cascade on the LIG biosensor

The effect of mediator (4-NA) concentration on cascade electron-transfer performance was investigated by varying its level from 10 to 50 mM (Fig. 4A–C). The highest sensitivity (9.21 µ A mM^{-1}) was obtained at 10 mM, whereas the sensitivity gradually decreased at concentrations above 20 mM. This behavior is interpreted as a result of the high mediator concentration causing diffusion limitation or disturbing the enzyme layer microstructure to reduce electron transfer. Accordingly, 10 mM was selected as the optimal mediator concentration, and the corresponding chronoamperometric responses and calibration curve are shown in Fig. 4B and C, respectively.

The effect of the PK:POx activity ratio on the cascade performance was investigated by tuning the ratio from 1:0.5 to 1:10 (Fig. 4D–F). The highest sensitivity (15.57 µA mM^{-1}) was confirmed at a PK:POx ratio of 1:3. In contrast, at the 1:10 ratio, where POx was in large excess, the CA failed to increase any more despite the increase in the K^+ concentration, and instead exhibited a pronounced plateau, leading to a substantial loss

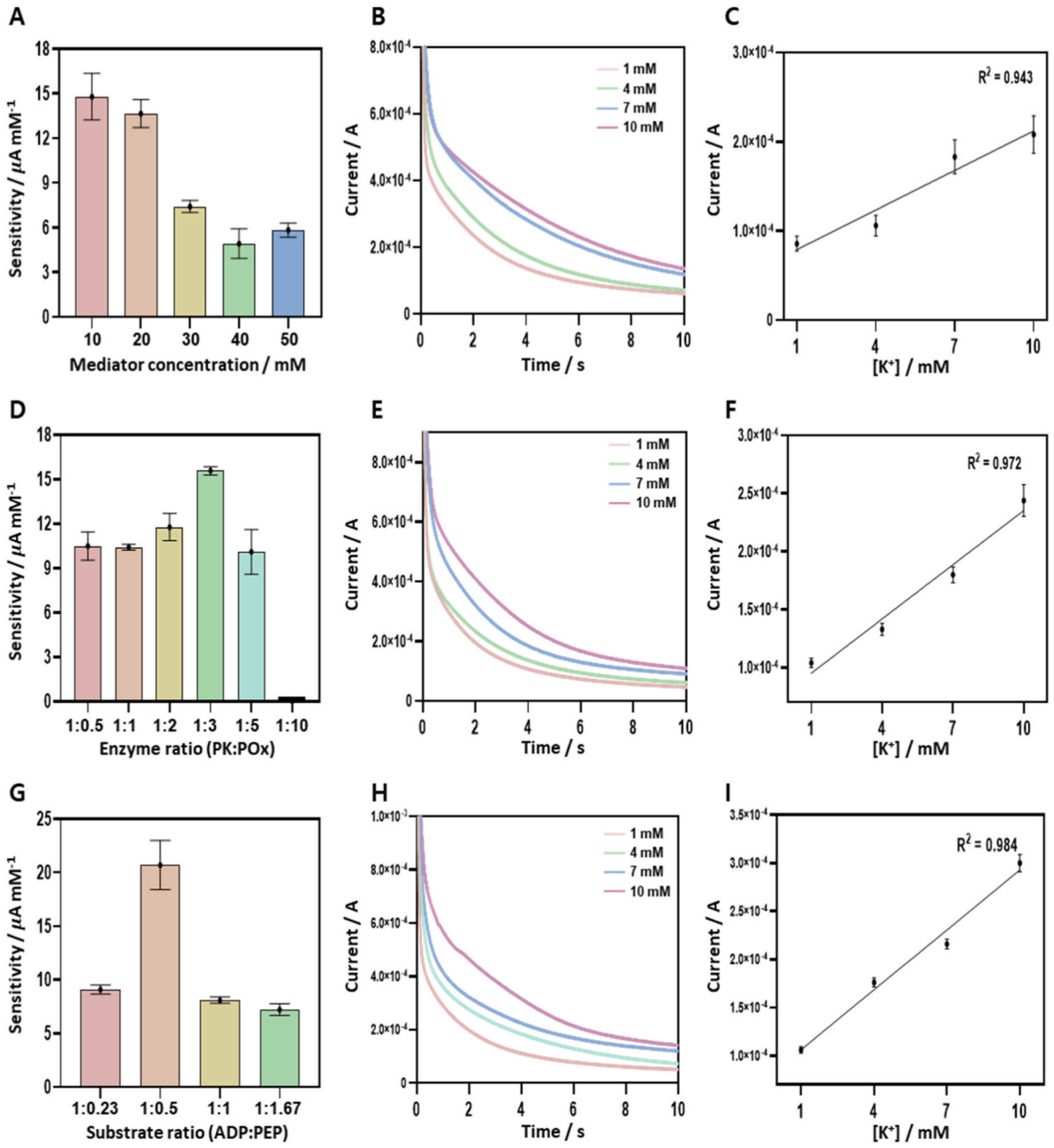

Fig. 4. Effects of mediator concentration, enzyme ratio, and substrate composition for the PK/POx/LIG K^+ amperometric biosensor.
(A) Sensitivity as a function of 4-nitrosoaniline (4-NA) mediator concentration (10-50 mM); (B) chronoamperometric (CA) responses at the optimal mediator concentration measured under 1, 4, 7, and 10 mM K^+; (C) calibration curve confirming 10 mM 4-NA as the optimal mediator level; (D) sensitivity obtained from varying PK:POx ratios (1:0.5, 1:1, 1:2, 1:3, 1:5, and 1:10); (E) CA responses measured at the optimal enzyme ratio; (F) corresponding calibration curve obtained under optimal PK:POx ratio; (G) sensitivity as a function of ADP/PEP substrate composition (1:0.23, 1:0.5, 1:1, and 1:1.67); (H) representative CA responses for each substrate ratio condition; and (I) calibration curve obtained under the optimal substrate composition.
*Error bars represent standard deviation (n = 4) from independently prepared biosensor strips.

of concentration dependence. This plateau may result from saturation of the downstream POx-mediated reaction step when the enzyme ratio is heavily shifted toward POx. Therefore, a ratio of 1:3 was adopted as the optimal enzyme composition, and the corresponding CA response and calibration curves are presented in Fig. 4E and F.

Finally, the effect of substrate composition (ADP:PEP) on the overall pyruvate flux was examined (Fig. 4G–I). Substrate concentrations were chosen to be approximately tenfold higher than K_m values, and the PEP concentration was varied to 0.7, 1.5, 3, and 5 mM at a fixed ADP concentration of 3 mM. The highest sensitivity (20.7 μA mM^{-1}) was obtained at an ADP:PEP ratio of 1:0.5, whereas unbalanced or excessive PEP conditions led to reduced reaction rates, lower pyruvate conversion efficiency, and a concomitant decrease in the amperometric response. The CA responses and calibration curves under these conditions are shown in Fig. 4H and I, respectively.

3.3. Electrochemical performance of the PK/POx/LIG potassium biosensor

The electrochemical performance of the PK/POx/LIG potassium biosensor was evaluated under the optimized conditions (4-NA 10 mM, PK:POx = 1:3, ADP:PEP = 1:0.5). Prior to K^+ sensing, the applied

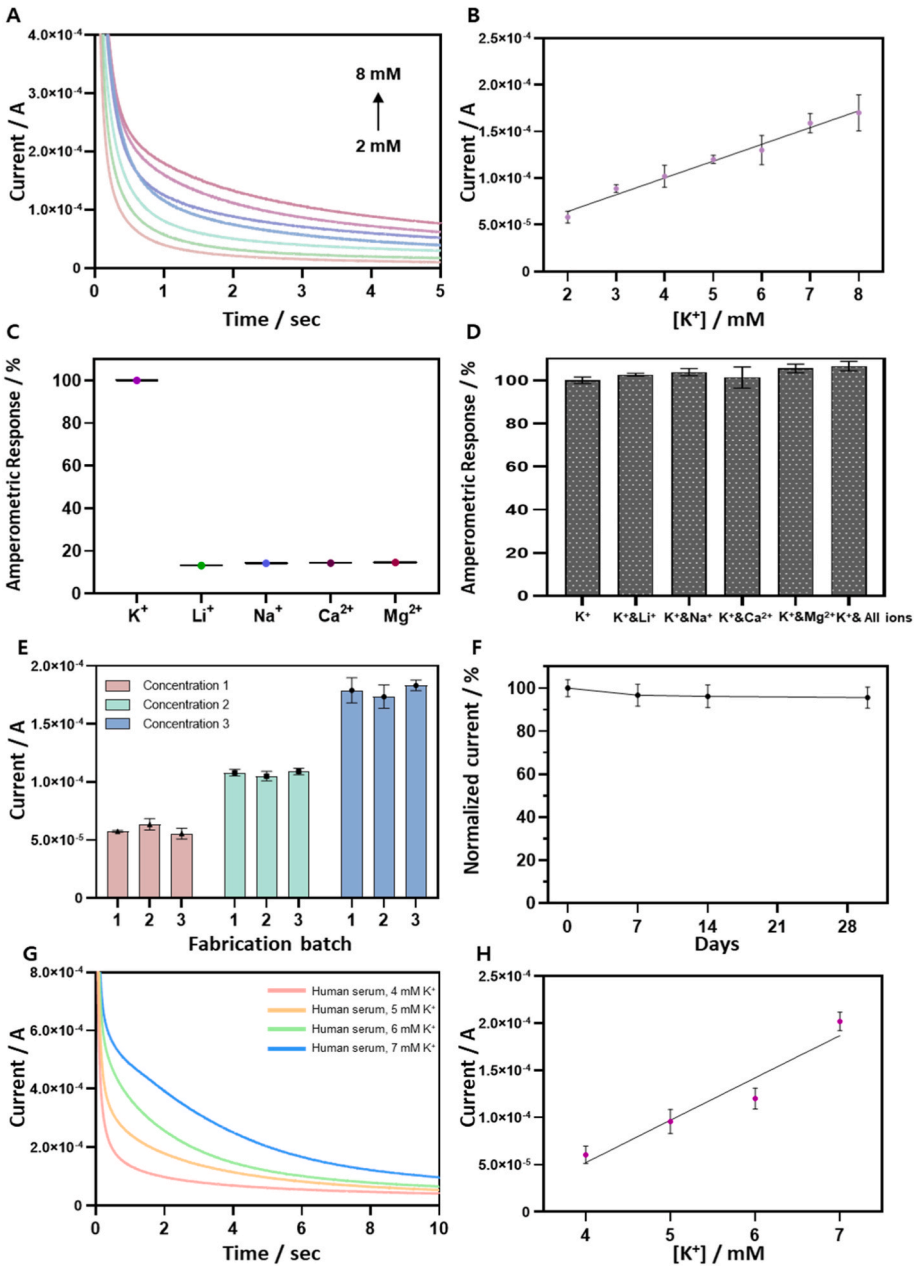

Fig. 5. Potassium sensing performance of the PK/POx/LIG amperometric biosensor.
(A) Chronoamperometric (CA) responses recorded under increasing K^+ concentrations; (B) calibration plot demonstrating linear response ($R^2 = 0.98$); (C) selectivity comparison against Li^+, Na^+, Ca^{2+}, and Mg^{2+}; (D) Selectivity evaluated as relative amperometric responses of each sample, expressed as a percentage of the K^+-only response (defined as 100%); (E) batch-to-batch reproducibility evaluated within three repeated measurements; (F) The current response at day 0 was defined as 100%, and the relative responses at 7, 14, and 30 days were normalized accordingly; (G) CA responses of real human serum samples and (H) corresponding calibration curve in the serum matrix ($R^2 = 0.94$).
*Error bars represent the standard deviation (n = 4 for B, F and H; n = 10 for E), measured using independently prepared sensor strips.

potential was optimized by linear sweep voltammetry (LSV) in a buffer solution containing KCl (Fig. S5). A distinct oxidation peak was observed at about 0.9 V, and considering the signal-to-noise ratio and background current, 0.9 V was selected as the operating potential for all subsequent chronoamperometric (CA) measurements.

Chronoamperometric measurements revealed a monotonic increase in current with increasing K^+ concentration (2-8 mM) (Fig. 5A). For quantitative analysis, the current measured at 5 s after potential application was used for calibration. The calibration curve (Fig. 5B) exhibited excellent linearity over this range, with a sensitivity of 18 μA mM^{-1} and a correlation coefficient (R^2) of 0.9833. The limit of detection (LOD), calculated as 3 σ/S using the standard deviation of the blank (σ) and the slope of the calibration curve (S) (Long and Winefordner, 1983), was determined to be 1.56 mM, which is sufficiently low to discriminate between normokalemic and hyperkalemic levels (Ghaderinezhad et al., 2020).

The ion-specific signal generation of the PK/POx/LIG biosensor was first examined by independently introducing individual cations under identical experimental conditions (Fig. 5C). Among the tested physiological cations, including Na^+, Li^+, Ca^{2+}, and Mg^{2+} (Kovesdy, 2017), only potassium ions induced a pronounced amperometric response, while the other cations produced negligible or no detectable current signals. This behavior reflects the intrinsic K^+-dependent activation mechanism of pyruvate kinase and confirms that the recorded current

Table 1
Comparison of potassium sensing platforms based on transduction principle and operational characteristics.

Composition of biosensing unit	Transduction principle	Membrane type	Stabilization time	Signal drift	Calibration requirement	Ref
Potentiometric						
Graphene-based solid-contact K^+ ISE	Equilibrium membrane potential (Nernstian response)	Polymer based (PVC)	60–100 s	12.6 ±1.1 μV/h potential drift (E_0 variation)	Required	(Ping et al., 2011)
Mxene-carbon fiber solid-contact K^+ ISE	Equilibrium membrane potential (Nernstian response)	Polymer based (PVC)	~200 s	mV level potential drift (E_0 variation)	Required	(Korolev et al., 2025)
Plasticizer-Free Silicone-Based K^+ ISE	Equilibrium membrane potential (Nernstian response)	Polymer based (Silicone elastomer)	Equilibrium-limited	27 ±18 μV/h potential drift (E_0 variation)	Required	(Spindler et al., 2023)
Amperometric						
PK/POx/LIG	Enzyme-kinetic, rate-governed amperometric transduction	Membrane-free (enzyme-kinetic transduction)	Defined current at 5 s (fixed-time kinetic readout)	Minimal (rate-governed current mode)	Not required at point of use (predefined assay conditions)	This work

originates from K^+-triggered enzymatic activity rather than nonspecific electrochemical processes.

To evaluate selectivity under competitive conditions, interference tests were performed using major physiological cations at identical concentration (Li^+, Ca^{2+}, Mg^{2+} at 1 mM; Na^+ at 140 mM) (Fig. 5D). Redox-active species such as uric acid, cysteine, and tyrosine induced negligible and non-sustained current responses (Fig. S6A), which is attributed to the enzyme-gated sensing mechanism. Together, these results demonstrate that the proposed biosensor exhibits both ionic and biochemical selectivity for potassium.

Reproducibility of the PK/POx/LIG biosensor was evaluated at two levels. As shown in Fig. 5E, sensors fabricated in different batches exhibited highly comparable current responses across the tested K^+ concentrations, indicating reliable and stable fabrication performance. Detailed sensor-to-sensor variation analysis using multiple individual electrode is provided in the Supporting Information (Fig. S6B).

Long-term operational stability of the PK/POx/LIG biosensor was evaluated by monitoring its amperometric response to potassium over a storage period of 30 days (Fig. 5F). The sensor retained more than 95% of its initial current response at 7, 14, and 30 days, indicating stable enzyme activity and interfacial electron transfer under the employed storage conditions.

Subsequently, the sensor performance was examined in a clinically relevant matrix to assess practical applicability. As shown in Fig. 5G, human serum samples spiked with potassium concentrations spanning 4–7 mM, corresponding to normokalemic to hyperkalemic levels, were analyzed using the PK/POx/LIG biosensor. Distinct and concentration-dependent current responses were observed across this clinically meaningful range (Fig. 5H), demonstrating that the enzymatic transduction mechanism remains effective even in complex biological media. The preserved signal separation between normal and elevated potassium levels indicates that the proposed biosensor is capable of reliable potassium discrimination under physiologically relevant serum conditions.

3.4. Comparison with equilibrium-based potentiometric potassium sensing

Conventional potentiometric potassium sensors generate analytical signals based on equilibrium potentials established across ion-selective membranes, which inherently follow the logarithmic response described by the Nernst equation (Eq. (1)):

$$E = E_0 + 2.303\frac{RT}{Z_A F} log\, a_x \quad \text{(Eq. 1)}$$

Where E is the equilibrium potential (**Δ** V), R the gas constant, T the temperature, Z_A the valence of the target ion, F Faraday's constant, and a_x the unknown activity on the other side of the membrane(Bakker et al., 1997; Francesca Criscuolo et al., 2021).

Consequently, accurate potentiometric measurements require sufficient equilibrium time and are susceptible to signal drift arising from membrane aging, ion redistribution, and environmental fluctuations, necessitating frequent calibration and stabilization procedures (Table 1).

In contrast, the present PK/POx/LIG biosensor operates under a fundamentally different, rate-governed transduction mechanism, in which the measured current is directly dictated by enzyme reaction kinetics rather than equilibrium potential formation. Upon potassium-dependent activation of pyruvate kinase, the resulting pyruvate flux drives the downstream oxidase reaction and mediator redox cycling, enabling rapid establishment of a steady-state current. Consistent with this mechanism, the chronoamperometric responses in this study reached stable current plateaus within a short time window and exhibited minimal baseline drift across independently prepared strips.

Importantly, the current-mode operation of the PK/POx/LIG platform is enabled by a set of tightly controlled assay conditions, including a fixed mediator concentration and substrate composition governing enzymatic kinetics, a standardized assay volume and predefined current acquisition window, and uniform electrode fabrication and enzyme immobilization protocols. Under these constraints, potassium concentration can be inferred directly from the measured current response without requiring sensor-specific calibration at the point of use. Taken together, this comparison highlights that the PK/POx/LIG platform circumvents key limitations of equilibrium-based potentiometric sensing by leveraging enzyme-kinetic signal transduction and rapid signal stabilization, thereby enabling fast and stable potassium monitoring that is particularly advantageous for POCT applications.

4. Conclusion

In this study, we developed an amperometric potassium biosensor that converts changes in extracellular K^+ concentration into electrochemical current signals through an enzyme-kinetic transduction mechanism based on a pyruvate kinase/oxidase (PK/POx) cascade integrated with a laser-induced graphene (LIG) electrode. By exploiting the intrinsic K^+-dependent activity of PK and 4-nitrosoaniline (4-NA)-mediated redox cycling, the proposed platform operates on principles fundamentally distinct from conventional potentiometric potassium sensors that rely on equilibrium potential responses. Systematic optimization of the mediator concentration, PK:POx enzyme ratio, and ADP:PEP substrate composition enabled reliable current-based potassium sensing over the physiological range (2-8 mM), with a sensitivity of 18 μA mM^{-1} and a detection limit of 1.56 mM. The sensor further demonstrated high selectivity against major physiological cations, excellent sensor-to-sensor reproducibility (RSD = 2.41-5.20%), and stable concentration-dependent signals in spiked human serum.

Beyond demonstrating potassium sensing performance, this study establishes an enzyme-kinetic, current-mode electrochemical sensing

framework in which ion concentration is transduced into a rate-governed current signal through controlled enzymatic kinetics. The robustness of this framework is supported by validated long-term storage stability, day-to-day signal reproducibility, and reliable operation in a complex serum matrix. Importantly, this sensing principle is not limited to potassium detection and can be extended to other ion-activated enzymatic systems, where specific ions regulate reaction kinetics and can be directly converted into measurable current signals (e.g., Na^{+}-dependent ATPases, Ca^{2+}-dependent kinases). Accordingly, the PK/POx/LIG platform provides a generalizable and practical foundation for point-of-use calibration-free electrochemical sensing under predefined and standardized assay conditions, offering a promising route toward next-generation POCT.

CRediT authorship contribution statement

Chaeeun Kim: Conceptualization, Data curation, Formal analysis, Investigation, Methodology, Validation, Visualization, Writing – original draft, Writing – review & editing. **Chaehyung Kim:** Formal analysis, Investigation. **Yujoon Kim:** Investigation. **Kangwon Lee:** Conceptualization, Funding acquisition, Resources, Supervision, Writing – review & editing.

Declaration of competing interest

The authors declare that they have no known competing financial interests or personal relationships that could have appeared to influence the work reported in this paper.

Acknowledgement

This research was supported by Korean Fund for Regenerative Medicine funded by Ministry of Science and ICT, and Ministry of Health and Welfare (25A0207L1, Republic of Korea).

Appendix A. Supplementary data

Supplementary data to this article can be found online at https://doi.org/10.1016/j.bios.2026.118572.

Data availability

Data will be made available on request.

References

Bakker, E., Bühlmann, P., Pretsch, E., 1997. Chem. Rev. 97, 3083–3132.
Bambang Kuswandi, R.A., Eka Pitaloka, Dian Ayu, Tri Murti, Bayu, Amrun Hidayat, Mochammad, 2025. Int. J. Electrochem. Sci. 20.
Baxter, R.M.G., Sarnowski, A., Dawson, A., Mason, H., Banerjee, D., 2022. Int. J. Nephrol. Renovascular Dis. 15, 215–228.
Datta, S., Christena, L.R., Rajaram, Y.R.S., 2013. 3 Biotech 3, 1–9.
Francesca Criscuolo, M.I.N.H., Taurino, Irene, Carrara, Sandro, De Micheli, Giovanni, 2021. IEEE Sens. J. 21.
Gao, J., He, S., Nag, A., 2021. Sensors 21, 2818.
Gao, W., Emaminejad, S., Nyein, H.Y.Y., Challa, S., Chen, K., Peck, A., Fahad, H.M., Ota, H., Shiraki, H., Kiriya, D., 2016. Nature 529, 509–514.
Geng, Z., Feng, Z., Kong, H., Su, J., Zhang, K., Li, J., Sun, X., Liu, X., Ge, L., Gai, P., 2024. Adv. Sci. 11, 2406843.
Ghaderinezhad, F., Ceylan Koydemir, H., Tseng, D., Karinca, D., Liang, K., Ozcan, A., Tasoglu, S., 2020. Sci. Rep. 10, 13620.
Gu, C., Zhang, L., Hou, T., Wang, Q., Li, F., Gai, P., 2025. Adv. Funct. Mater., 2423106
Hutter, T., Collings, T.S., Kostova, G., Frankl, F.E.K., 2022. Sens. Diagn. 1, 614–626.
Jian Lin, Z.P., Liu, Yuanyue, Ruiz-Zepeda, Francisco, Ye, Ruquan, Samuel, Errol L.G., Jose Yacaman, Miguel, Yakobson, Boris I., Tour, James M., 2014. Nat. Commun. 5.1 (5714).
Kim, Changheon, Hong, Changgi, Lee, Kangwon, 2021. Biosens. Bioelectron. 181.
Korolev, I., Bondar, A., Pavlova, A., Maleeva, K., Minisheva, V., Ovinov, G., Skorb, E.V., Smirnov, E., 2025. Small, e10942.
Kovesdy, C.P., 2017. Rev. Endocr. Metab. Disord. 18, 41–47.
Gyubok Lee, C.K., Kim, Dongwoo, Hong, Changgi, Kim, Taeyong, Lee, Moongoo, Lee, Kangwon, 2022. ACS Omega 7, 40973–40982.
Lee, Kangwon, Polich, LK, Kim, Jinsang, 2010. Analyst 135 (9), 2179–2189.
Lee, H., Reginald, S.S., Sravan, J.S., Lee, M., Chang, I.S., 2025. Trends Biotechnol. 43, 1328–1355.
Liu, X., Cheng, H., Zhao, Y., Wang, Y., Li, F., 2022. Biosens. Bioelectron. 199, 113906.
Liu, X., Gao, X., Yang, L., Zhao, Y., Li, F., 2021. Anal. Chem. 93, 11792–11799.
Long, G.L., Winefordner, J.D., 1983. Anal. Chem. 55, 712A–724A.
Luong, D.X., Yang, K., Yoon, J., Singh, S.P., Wang, T., Arnusch, C.J., Tour, J.M., 2019. ACS Nano 13 (2), 2579–2586.
Ma, D., Ghoreishizadeh, SS., Georgiou, P., 2021. IEEE Sens. 21, 5720–5727.
Marc Parrilla, M.C., Crespo, Gaston A., 2019. TrAC, Trends Anal. Chem. 110, 303–320.
Mingyang Liu, G.Z., Yang, Cheng, Wang, Han, Cheng, Jing, 2023. Adv. Mater. Interfac. 10.
Movaghgharnezhad, S., Kang, P., 2024. J. Mater. Chem. C 12, 6718–6742.
Oria-Hernández, J., Cabrera, N., Pérez-Montfort, R., Ramírez-Silva, L., 2005. J. Biol. Chem. 280, 37924–37929.
Pant, V., 2022. Ejifcc 33, 56–62.
Park, C.H., Kim, Y., Kim, C., Kim, C., Kim, S., Lee, K., Yoo, T.H., 2025. Clin. J. Am. Soc. Nephrol. 21, 425–436.
Ping, J., Y. Wang, J. Wu and Y. Ying (2011). 13, 1529-1532.
Sassolas, A., Leca-Bouvier, Béatrice D., Blum, Loïc J., 2008. Chem. Rev. 108, 109–139.
Spindler, B.D., Graf, K.I., Dong, X.I., Kim, M., Chen, X.V., Buhlmann, P., Stein, A., 2023. Anal. Chem. 95 (33), 12419–12426.
Tehrani, F., Bavarian, B., 2016. Sci. Rep. 6, 27975.
Viera, A.J., Wouk, N., 2015. Am. Fam. Physician 92, 487–495.
Wang, J., 2006. Biosens. Bioelectron. 21, 1887–1892.
Yang, Z., Qi, C., Zheng, X., Zheng, J., 2015. New J. Chem. 39, 9358–9362.
Ye, R., James, D.K., Tour, J.M., 2019. Adv. Mater. 31, e1803621.
Zacchia, M., Abategiovanni, M.L., Stratigis, S., Capasso, G., 2016. Kidney Dis (Basel) 2, 72–79.